Available online at www.sciencedirect.com
ScienceDirect
Trans. Nonferrous Met. Soc. China 35(2025) 243−256
Transactions of Nonferrous Metals Society of China
www.tnmsc.cn

Improved rate and cycling performances of $Na_3V_2(PO_4)_2F_2O$ by $Ti^{3+/4+}$ doping with two oxidation states for sodium cathodes

Xiao-fei SUN[1,2,3], Anastase NDAHIMANA[1,2,3], Ling-zhi WANG[1,2], Zi-kang WANG[1,2], Quan-sheng LI[1,3], Wei TANG[4], Min-xing YANG[2,3], Xue-song MEI[1,2,3]

1. State Key Laboratory for Manufacturing System Engineering, Xi'an Jiaotong University, Xi'an 710049, China;
2. School of Mechanical Engineering, Xi'an Jiaotong University, Xi'an 710049, China;
3. Shaanxi Key Laboratory of Intelligent Robots, Xi'an Jiaotong University, Xi'an 710049, China;
4. School of Chemical Engineering and Technology, Xi'an Jiaotong University, Xi'an 710049, China

Received 7 May 2023; accepted 8 December 2023

Abstract: Ti at the oxidation states of Ti^{3+} and Ti^{4+}, was used to enhance the performance of $Na_3V_2(PO_4)_2F_2O$ by partially substituting vanadium. After doping Ti, the crystallographic volume is decreased due to the less radii of $Ti^{3+/4+}$, and the valence of Ti is demonstrated identical to V. During sodium insertion in Ti-doped $Na_3V_2(PO_4)_2F_2O$, the two discharge plateaus split into three because of the rearrangement of local redox environment. Consequently, the optimized $Na_3V_{0.96}Ti_{0.04}(PO_4)_2F_2O$ shows a specific capacity of 123 and 63 mA·h/g at 0.1*C* and 20*C*, respectively. After 350 cycles at 0.5*C*, the capacity is gradually reduced corresponding to a retention of 71.05%. The significantly improved performance is attributed to the rapid electrochemical kinetics, and showcases the strategy of replacing $V^{3+/4+}$ with $Ti^{3+/4+}$ for high-performance vanadium-based oxyfluorophosphates.

Key words: sodium vanadium oxyfluorophosphate; titanium doping; cathode; sodium battery; energy storage

1 Introduction

Electrical energy storage is critical for the development and application of renewable solar/ wind-based energy sources due to its inherent inconsistency [1,2]. Lithium-ion battery (LIB) has been widely used in portable electronic devices, electric vehicles, and power stations since the time of its commercialization [3−5]. However, its vast utilization has been restricted by the low lithium reserve in the earthcrust, and thus the high cost of LIBs. Therefore, it is essential to explore high-performance low-cost battery technologies for the long-term viability of sustainable energy systems [6,7].

Sodium-ion battery (SIB) is considered such a technology for large-scale energy storage because of the abundance of sodium in the earth and the inexpensive cost of SIBs [8]. SIB has a battery structure and working principle similar to LIB, but currently has inferior electrochemical performance due to the larger ionic radius and thus sluggish Na^+ diffusivity in the battery [9,10]. Therefore, many efforts have been dedicated to developing good cathode materials with stable structures and efficient Na^+ diffusivities. So far to date, transition metal oxides [11], organic materials [12], Prussian blue analogs [13], and polyanion compounds [14] have attracted a lot of attention.

As a polyanionic cathode material, Na^+ superionic conductor (NASICON) $Na_3V_2O_{2y}(PO_4)_2$-

Corresponding author: Xiao-fei SUN, Tel: +86-29-82663870, E-mail: xfsunxjtu@mail.xjtu.edu.cn;
Wei TANG, Tel: +86-29-82663870, E-mail: tangw2018@mail.xjtu.edu.cn
https://doi.org/10.1016/S1003-6326(24)66677-X

F_{3-2y} ($0\le 2y<3$) has great potential for its outstanding structure stability, large theoretical capacity and high working voltage [15,16]. It is constituted of corner-sharing $V(O,F)_6$ octahedra (VO_5F or VO_4F_2) and PO_4 tetrahedra with a three-dimensional tunnel framework for Na^+ diffusion, and therefore has superior thermodynamic stability in comparison with other cathode materials of SIBs [17]. However, the electronic and ionic conductivities are naturally low because of the polyanionic framework, severely restraining the rate and cycling performances of this class of materials [18]. The practical battery performance is also affected by the irreversible phase transition during partial (de)sodiation redox reactions [19].

Therefore, it is important to improve the electric conductivity and to overcome these drawbacks of $Na_3V_2O_{2y}(PO_4)_2F_{3-2y}$ ($0\le 2y<3$). Various strategies such as composition tuning [20], surface coating [21], and ionic doping [22,23] have been widely attempted. Heterogeneous cation doping could adjust the octahedral and tetrahedral sites and the charge balance of the host structure, and is an effective way to enhance the intrinsic electric conductivity and the (de)sodiation redox kinetics [24−26]. Consequently, the electrochemical performance of the cathode material can be improved. For instance, Al-doped $Na_3V_{1.93}Al_{0.0.07}$-$(PO_4)_2F_3$ could deliver a specific capacity of 121 and 57 mA·h/g at 0.1*C* and 10*C*, respectively [27]. The kinetic response of $Na_3V_2(PO_4)_2F_3$ at high rates is also improved by Cr doping [28]. YUE et al [29] prepared $Na_3V_{1.85}Fe_{0.15}(PO_4)_2O_2F$ micro cuboids combining hydrothermal synthesis with Fe doping, which shows a specific capacity of 60 mA·h/g at a high rate of 20*C*.

In this work, Ti doping is used to improve further the electrochemical performance of high-capacity $Na_3V_2(PO_4)F_2O$ (NVPFO) which were previously reported [30], so as to develop practically high-safety, high-energy, high-power and long-life cathode materials for SIBs. Although Ti has been applied to enhancing the performance of several electrode materials for LIBs and SIBs [31,32], the effect of Ti doping on the structure and electrochemical performance of NVPFO has not been revealed. Given the valence of V (i.e., V^{3+} and V^{4+}) in NVPFO, Ti with identical oxidation states to V (i.e., Ti^{3+} and Ti^{4+}) is designed in this work to partially substitute V. A variety of NVPFO samples with different amounts of Ti doping are simply prepared following a facile solid-state approach, and the crystal structure, particle size/morphology, surface composition, battery performance and electrochemical kinetics are comparatively studied to obtain the optimized doping amount with the best performance, and to understand the beneath mechanism of Ti doping.

2 Experimental

2.1 Materials preparation

Ti-doped $Na_3V_{2-x}Ti_x(PO_4)_2F_2O$ ($0\le x<1$) were prepared following a solid-state sintering route as previously reported [30]. In the first step, stoichiometric NH_4VO_3, $NH_4H_2PO_4$, TiO_2, and carbon were ball-milled and calcined at 750 °C for 4 h in an argon (Ar) atmosphere to obtain the intermediate $V_{1-x}Ti_xPO_4$, while the intermediate $VOPO_4$ was synthesized by mixing NH_4VO_3 and $NH_4H_2PO_4$ in stoichiometry and then heating at 750 °C for 4 h under air. In the second step, stoichiometric $V_{1-x}Ti_xPO_4$, $VOPO_4$, Na_2CO_3, and NaF were mixed uniformly by ball-milling in alcohol and pressed into tablets after drying, which were then sintered at 650 °C under Ar flow for 4 h. The detailed process can be found in the reference [30].

2.2 Structure and morphology characterization

X-ray diffraction (XRD) was conducted using X'Pert Pro-PANanalytical with the monochromatic Cu K_α radiation. The scanning 2θ range was 10°−80°. Rietveld refinements on the XRD patterns were carried out by the High-score plus program. X-ray photoelectron spectroscopy (XPS) was performed on an AXIS ultra DLD, and the spectra were analyzed by the Avantage package. The particle size and morphology were observed by a scanning electron microscope (SEM, Hitachi S-4800) equipped with energy dispersive spectroscopy (EDS). The particle size was further precisely acquired by the Nano-Measurer 1.2.5 analyzer. Transmission electron microscopy (TEM, JEM 2100) was utilized to get an in-depth understanding of the particle structure, and Raman spectra were collected by a Horiba LabSpec 6 with a 532 nm laser excitation.

2.3 Electrochemical measurements

The electrochemical performances of $Na_3V_{2-x}Ti_x(PO_4)_2F_2O$ ($0\le x<1$) were measured using standard CR2016 coin cells with lithium metal anodes. The working electrodes were constituted of 70 wt.% $Na_3V_{2-x}Ti_x(PO_4)_2F_2O$, 20 wt.% Super P, and 10 wt.% polyvinylidene fluoride (PVDF), which were dispersed in *N*-methyl-2-pyrrolidone (NMP) to form homogeneous slurries. The slurries were then deposited on the pre-cleaned aluminum foils using a MSK-AFA-III automatic film coater followed by drying in a vacuum oven at 120 °C for 12 h. Such electrodes were cut into round discs with the diameter of 12 mm to fabricate CR2016 cells, and Celgard 2500 polypropylene and 1 mol/L $NaClO_4$ solution in EC−DEC (ethylene carbonate−diethyl carbonate) served as the separator and electrolyte, respectively. The prototype cells were assembled in an Ar-filled glove box with the contents of oxygen and water both below 10^{-7}.

The charge/discharge, rate and cycling performances were tested in the galvanostatic mode using a Neware battery test system (CT-4008) at room temperature in the voltage range of 2.0−4.5 V (vs Na^+/Na, hereafter). Electrochemical impedance spectroscopy (EIS) and cyclic voltammetry (CV) were measured by a Versatile Multichannel PMC 1000 workstation (Princeton). The frequency range for EIS was between 0.01 Hz and 100 kHz. The scanning rate for CV was 0.1 mV/s. The galvanostatic intermitted titration technique (GITT) with a stepwise of 10 min was employed to analyze the electrochemical kinetics and Na^+ diffusion coefficients.

3 Results and discussion

3.1 Chemical structure

Ti-doped $Na_3V_{2-x}Ti_x(PO_4)_2F_2O$ ($0\le x<1$, at.%) with four different doping amounts (x=0, 0.02, 0.04, 0.06) were designed and prepared according to various fundamental research on $Na_3V_2O_{2y}(PO_4)_2F_{3-2y}$ ($0\le 2y<3$) as well as Ti doping research on different energy storage materials [33,34]. The structure, morphology and electrochemical performance are comparatively studied in this work. The phase structures of $Na_3V_{2-x}Ti_x(PO_4)_2F_2O$ (x= 0.02, 0.04, 0.06) identified by XRD are shown with the phase structure of pristine NVPFO in Fig. 1(a). All the diffraction peaks have comparable intensities and positions indexed to tetragonal $Na_3V_2(PO_4)_2F_2O$ in the space group $P4_2/mnm$. No detectable impurity peak is observed for all the samples, indicating no obvious phase change after Ti doping. Rietveld refinement is used to fit the XRD patterns accurately and to calculate the lattice parameters, and the results are shown in Figs. 1(b−e) and Table 1. All the refinements have a good fitting as all the R_p and R_{wp} are small and reliable. The lattice parameters of a, b, c and cell volume (V) clearly decrease with the increase of doping amount because of the smaller radii of Ti^{3+} and Ti^{4+} in comparison with those of V^{3+} and V^{4+} [33,34]. According to the XRD refinements, it is worth noting that the occupancy of the Na(2) site is slightly decreased upon the increasing of Ti doping, i.e., a very small number of vacancies may be induced, suggesting that Na^+ migration in NVPFO could potentially be facilitated [35].

Figure 2 shows the XPS spectrum of Ti-doped $Na_3V_{1.96}Ti_{0.04}(PO_4)_2F_2O$ in comparison with that of pristine NVPFO. All the characteristic peaks of C 1s, Na 1s, V 2p, P 2p, O 1s, F 1s, and Ti 2p are indicated in the survey spectra (Fig. 2(a)). The high-resolution V 2p spectrum of NVPFO is shown in Fig. 2(b). With good fitting, V^{3+} $2p_{1/2}$ and V^{3+} $2p_{3/2}$ are posited at 523.21 and 516.46 eV, respectively, while V^{4+} $2p_{1/2}$ and V^{4+} $2p_{3/2}$ are located at 524.37 and 517.31 eV, respectively [36]. The V 2p spectrum of $Na_3V_{1.96}Ti_{0.04}(PO_4)_2F_2O$ is magnified in Fig. 2(c), and the fitting results are in good agreement with pristine NVPFO. The binding energies of Ti 2p are recorded and fitted, as shown in Fig. 2(d). The peaks at 463.41 and 458.54 eV correspond to Ti^{3+} $2p_{1/2}$ and Ti^{3+} $2p_{3/2}$, respectively, while those at 464.63 and 459.16 eV are in good accordance with Ti^{4+} $2p_{1/2}$ and Ti^{4+} $2p_{3/2}$, respectively [32]. Therefore, Ti is verified in two oxidation states, i.e., Ti^{3+} and Ti^{4+}, identical to V^{3+} and V^{4+} of V in the host structure. Thus, it is beneficial to charge balance, electric conductivity and structural stability after heterogeneous doping.

3.2 Particle morphology

The particle morphology and particle size are analyzed by SEM and TEM. Figures 3(a−d) show the SEM image of each sample with a particle size distribution histogram on the right. It can be seen that the unregular particle shape is not obviously affected after Ti doping, and the particle size is

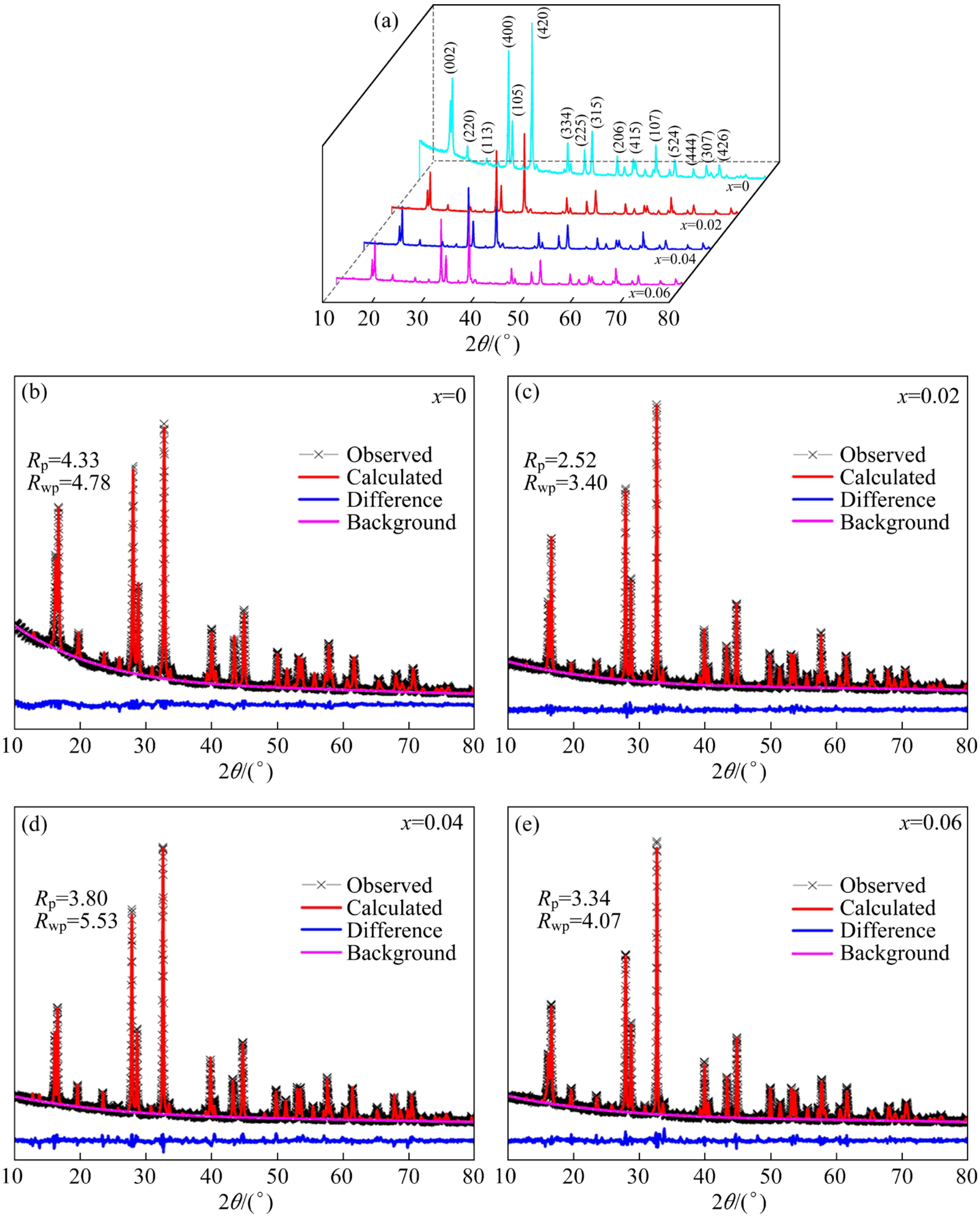

Fig. 1 XRD patterns with Rietveld refinements of $Na_3V_{2-x}Ti_x(PO_4)_2F_2O$ ($0 \le x < 1$)

Table 1 Lattice parameters of $Na_3V_{2-x}Ti_x(PO_4)_2F_2O$ ($0 \le x < 1$) obtained from XRD refinements

Sample	a/Å	b/Å	c/Å	V/Å^3
x=0	9.0334	9.0334	10.6629	870.117
x=0.02	9.0309	9.0309	10.6612	869.497
x=0.04	9.0297	9.0297	10.6590	869.087
x=0.06	9.0279	9.0279	10.6512	868.104

statistically 1.28−1.39 μm. The EDS mapping on the selected area of the SEM image of $Na_3V_{1.96}Ti_{0.04}(PO_4)_2F_2O$ is shown in Fig. 4. All the elements such as Na, V, P, O, F, and especially Ti are successfully mapped with uniform distributions. Hence, in good agreement with XRD and XPS, EDS confirms Ti doping into NVPFO again. The TEM images of pristine NVPFO and $Na_3V_{1.96}Ti_{0.04}(PO_4)_2F_2O$ are shown in Figs. 5(a, b), respectively. The lattice spacings of 0.338 and 0.508 nm corresponding to the interplanar (107) and (220) planes of $Na_3V_2(PO_4)_2F_2O$ are well observed, in good consistency with the XRD results (Fig. 1) and literature [37]. An amorphous carbon layer of roughly 6.61−6.94 nm is observed on the

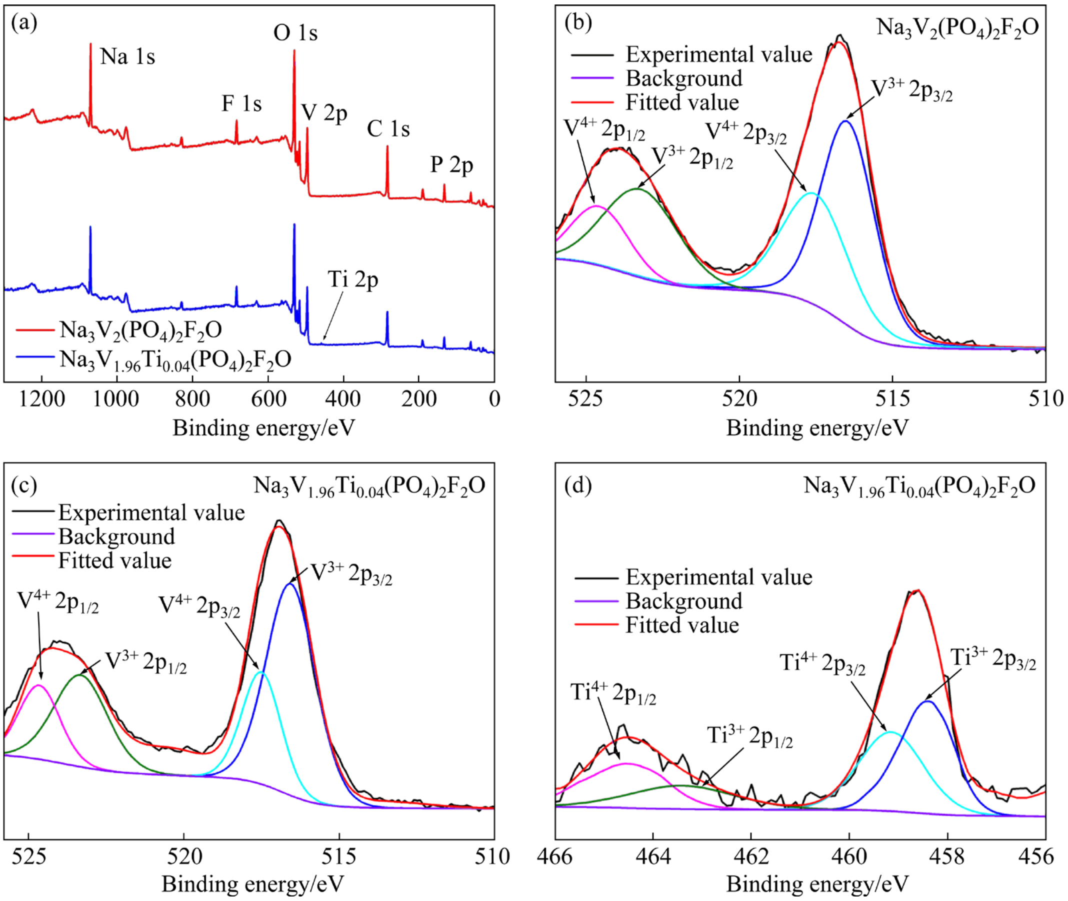

Fig. 2 XPS survey spectra of $Na_3V_{2-x}Ti_x(PO_4)_2F_2O$ (x=0, 0.04) (a); High-resolution XPS spectra of V 2p for $Na_3V_2(PO_4)_2F_2O$ (b); High-resolution XPS spectra of V 2p (c) and Ti 2p (d) spectra for $Na_3V_{1.96}Ti_{0.04}(PO_4)_2F_2O$

particle surface of both samples due to the residual carbon after calcination [38]. The carbon structure is further characterized by Raman spectroscopy, and the results are displayed in Fig. 5(c). As widely recognized [39], the two distinct peaks at 1348 and 1600 cm^{-1} correspond to the D-band (defective carbon) and G-band (graphite carbon), respectively. The similar intensity ratio of I_D/I_G indicates no obvious change in the structure of residual carbon after Ti doping. Therefore, the particle shape, size and carbon form are generally not affected by Ti doping, and the coming difference in electrochemical performance should be mainly ascribed to the changes in crystallographic structure and electric (including ionic) conductivity caused by Ti doping.

3.3 Battery performance

The electrochemical performances of $Na_3V_{2-x}Ti_x(PO_4)_2F_2O$ (x=0, 0.02, 0.04, 0.06) are measured by standard CR2016 cells with lithium anodes. The charge/discharge curves at 0.1C are depicted in Figs. 6(a−d), and the corresponding cyclic voltammograms at 0.1 mV/s are shown on the right of each figure. Two redox pairs (i.e., charge/discharge plateaus) located at 3.83/3.34 V and 4.17/3.87 V are presented for pristine $Na_3V_2(PO_4)_2F_2O$, in good agreement with previous reports [40]. However, a discharge plateau roughly at 3.24−3.33 V is clearly shown in Ti-doped samples, and the corresponding CV curves prove well the split of the reduction peak at the lower voltage. This might be caused by the rearrangement of the local redox environment as some Na^+ could shift from the Na(1) site to the Na(2) site during electrochemical redox reaction [41], since a very small amount of Na(2) vacancies are created after Ti doping, as already discussed by XRD refinements. The typical specific discharge capacity at 0.1C is 133, 124, 123, and 119 mA·h/g when the doping amount is 0, 0.02, 0.04, and 0.06, respectively. The reasons for capacity decrease along with increasing doping may come from the decrease of electrochemically active V that is

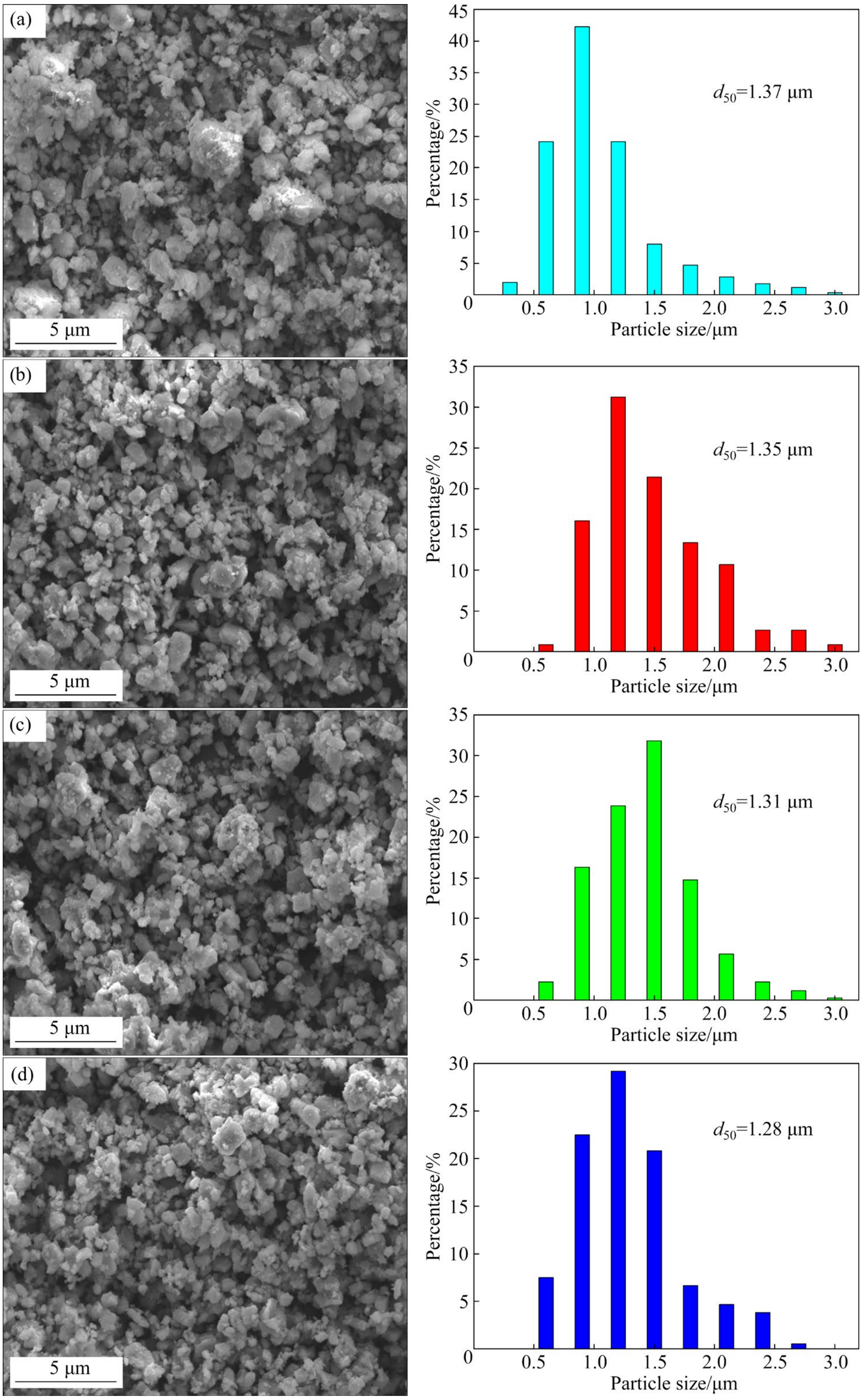

Fig. 3 SEM images of $Na_3V_{2-x}Ti_x(PO_4)_2F_2O$ when x=0 (a), 0.02 (b), 0.04 (c) and 0.06 (d) (The particle size distribution of each sample is shown on the right of its SEM image)

substituted by Ti. Therefore, the doped Ti is inactive although it has two oxidation states (Ti^{3+} and Ti^{4+}). Nonetheless, the polarization between charge and discharge hysteresis is noticeably reduced after Ti doping, and $Na_3V_{1.96}Ti_{0.04}(PO_4)_2F_2O$ with 2 at.% doping shows the smallest polarization compared with pristine NVPFO and other doping amounts, as indicated by the CV curves.

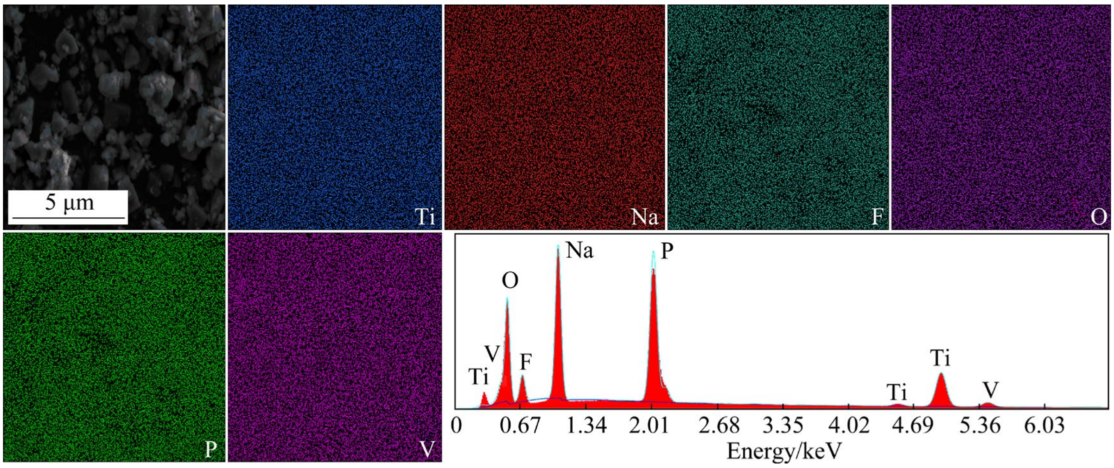

Fig. 4 EDS mapping of $Na_3V_{1.96}Ti_{0.04}(PO_4)_2F_2O$

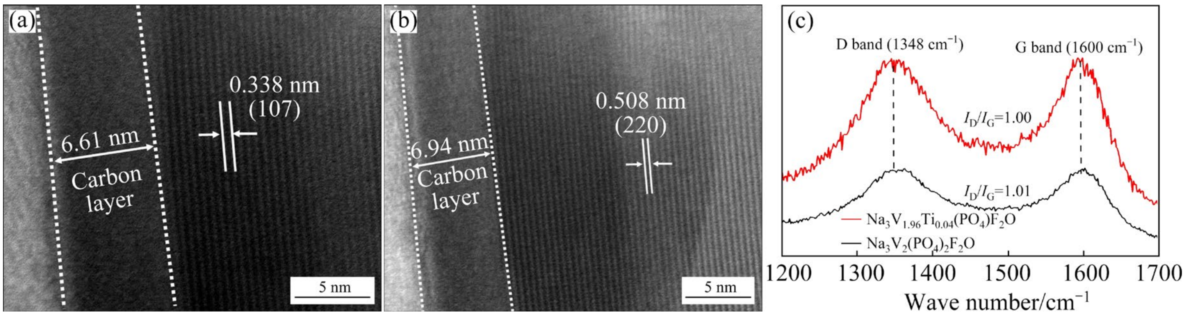

Fig. 5 TEM images of $Na_3V_2(PO_4)_2F_2O$ (a) and $Na_3V_{1.96}Ti_{0.04}(PO_4)_2F_2O$ (b), and their comparison in Raman spectrum (c)

The rate and cycling performances of $Na_3V_{2-x}Ti_x(PO_4)_2F_2O$ (x=0, 0.02, 0.04, 0.06) are measured with galvanostatic charge/discharge at constant current densities. Figure 7(a) compares the specific discharge capacities of different samples at various currents to evaluate their rate capability. As discussed, Ti-doped materials have slightly decreased capacities at very low rates such as 0.1C. However, when x=0.04, and the $Na_3V_{0.96}Ti_{0.04}(PO_4)_2F_2O$ shows remarkably improved capacities at rates higher than 0.2C, and thus it has the fastest charge/discharge ability among all the samples. The specific capacity of $Na_3V_{0.96}Ti_{0.04}(PO_4)_2F_2O$ at 0.1C, 0.2C, 1C, 4C, 20C, and 60C is 123, 115, 101, 84, 63, and 51 mA·h/g, respectively. About 41.46% of the capacity is retained when the charge/discharge rate is increased 600 times from 0.1C to 60C. On the contrary, the specific capacity of pristine NVPFO is 133, 112, 91, 69, 41, and 25 mA·h/g at 0.1C, 0.2C, 1C, 4C, 20C, and 60C, respectively. Only 18.80% of the capacity is retained when the charge/discharge rate is increased from 0.1C to 60C. Figure 7(b) displays the specific discharge capacities of $Na_3V_{2-x}Ti_x(PO_4)_2F_2O$ (x=0, 0.02, 0.04, 0.06) upon long-term cycling at 0.5C. Again, $Na_3V_{0.96}Ti_{0.04}(PO_4)_2F_2O$ shows the highest specific capacity as well as the most stable capacity retention along with cycling. The capacity gradually decreases from 114 to 81 mA·h/g after 350 cycles, indicating a capacity retention of 71.05% and a capacity loss of 0.08% per cycle. In comparison, the capacity of pristine NVPFO is decreased from 106 to 64 mA·h/g with a retention of only 60.38% after 350 cycles. The outstanding rate and cycling performances of the optimized $Na_3V_{1.96}Ti_{0.04}(PO_4)_2F_2O$ are also compared with relevant family materials reported in recent literature. It can be seen from Table 2 that $Na_3V_{1.96}Ti_{0.04}(PO_4)_2F_2O$ in this work exhibits superior electrochemical performance, and is practically a promising cathode material for SIBs. One needs to note that the electrode loading density of $Na_3V_{1.96}Ti_{0.04}(PO_4)_2F_2O$ in this work is 2.2−2.6 mg/cm^2, which is comparable and even higher than that typically reported in most literature in Table 2. In addition, the charge/discharge curves of the first and last (350th) cycle during the cycling

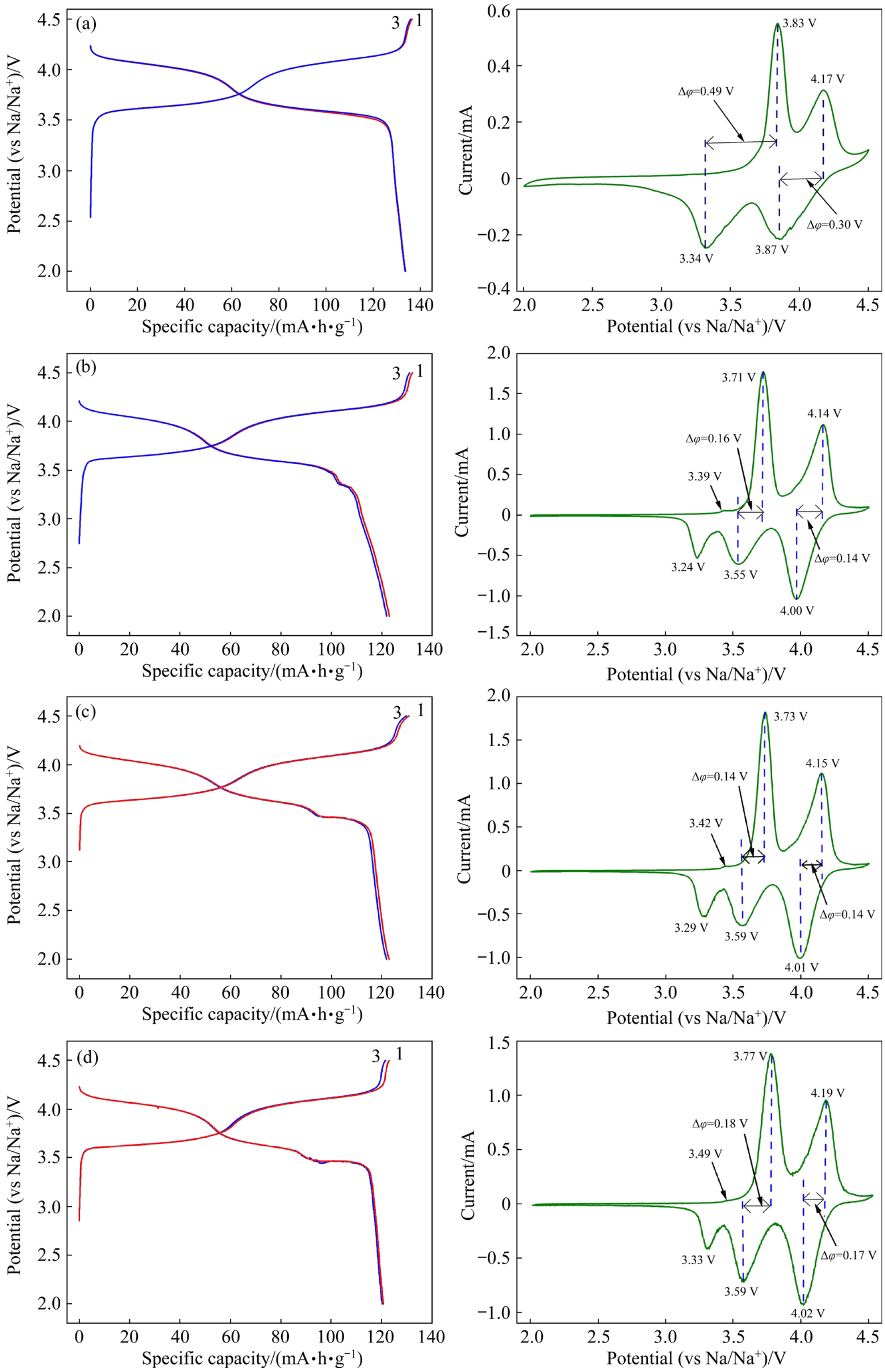

Fig. 6 Charge/discharge curves of $Na_3V_{2-x}Ti_x(PO_4)_2F_2O$ at 0.1*C* rate with *x* of 0 (a), 0.02 (b), 0.04 (c) and 0.06 (d) (The corresponding CV profiles are shown on right)

of $Na_3V_{2-x}Ti_x(PO_4)_2F_2O$ (x=0, 0.02, 0.04, 0.06) are ploted, and the results are shown in Figs. 7(c, d), respectively. Although the profiles are very similar in each figure, $Na_3V_{1.96}Ti_{0.04}(PO_4)_2F_2O$ has the smallest polarization throughout the whole cycling and is thus anticipated to possess boosted electrochemical redox kinetics during charging/ discharging.

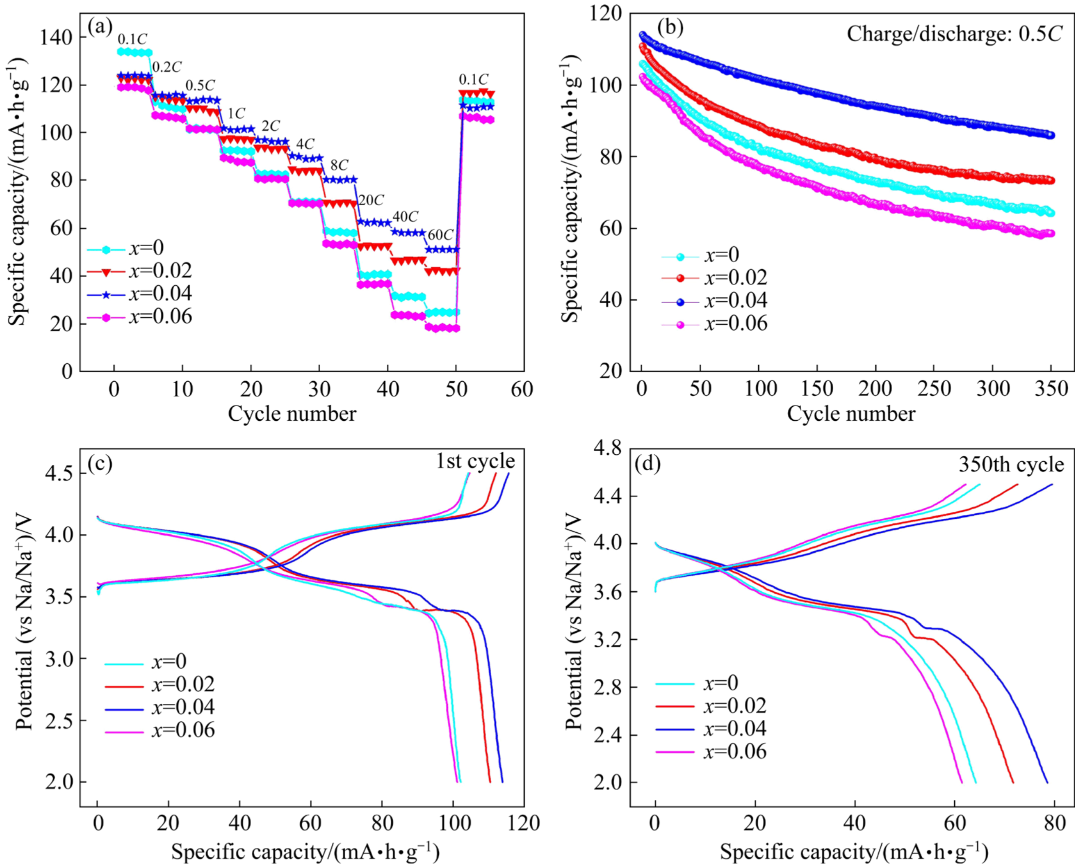

Fig. 7 Rate (a) and cycling (b) performances of $Na_3V_{2-x}Ti_x(PO_4)_2F_2O$ ($0\le x<1$), and their comparison in charge/discharge curves before (c) and after (d) cycling

Table 2 Comparison in electrochemical performance of $Na_3V_{1.96}Ti_{0.04}(PO_4)_2F_2O$ with recent literature

Material	Synthesis method	Rate performance	Cycling performance	Ref.
$Na_3V_{1.96}Ti_{0.04}(PO_4)_2F_2O$	Solid state	123 mA·h/g @ 0.1*C* 101 mA·h/g @ 1*C* 97 mA·h/g @ 2*C* 63 mA·h/g @ 20*C*	71.05% after 350 cycles at 0.5*C*	This work
$Na_3V_{2-x}La_x(PO_4)_2F_3$ ($0<x<1$)	Solid state	100 mA·h/g @ 0.1*C* 76 mA·h/g @ 2*C*	–	[42]
$Na_3V_2(PO_4)_3$/C·$Na_3V_2(PO_4)_2F_3$/C @rGO	Sol−gel	123 mA·h/g @ 0.1*C*	88.3% after 100 cycles at 5*C*	[43]
$Na_3V_2O_{2x}(PO_4)_2F_{3-2x}$/C ($0<x<1$)	Hydrothermal	99 mA·h/g @ 0.1*C* 91 mA·h/g @ 1*C* 86 mA·h/g @ 2*C*	95% after 200 cycles at 1*C*	[18]
$Na_3V_2(PO_4)_2F_2O$	Solid state	88 mA·h/g @ 2*C*	58.2% after 275 cycles at 1*C*	[30]
$Na_3V_2(PO_4)_2O_2F$-MWCNT	Hydrothermal	110 mA·h/g @ 0.1*C* 87 mA·h/g @ 1*C* 82 mA·h/g @ 2*C*	89.1% after 120 cycles at 0.1*C*	[44]
$Na_3V_2(PO_4)_2O_2F$@rGO	Hydrothermal	87 mA·h/g @ 0.1*C* 81 mA·h/g @ 1*C* 46 mA·h/g @ 20*C*	95% after 100 cycles at 1*C*	[45]

3.4 Electrochemical kinetics

The electrochemical kinetics is evaluated by EIS and GITT. The EIS Nyquist plots of $Na_3V_{2-x}Ti_x(PO_4)_2F_2O$ (x=0, 0.02, 0.04, 0.06) are presented in Fig. 8(a). All the spectra consist of a depressed semicircle in the high-frequency region and a straight slope line in the low-frequency region. An equivalent circuit model of R_s+(CPE//(R_{ct}+Z_w)) as shown in the inset of Fig. 8(a) is used to fit the Nyquist spectra. In this circuit, R_s represents the ohmic contact resistance, CPE is a constant phase element, R_{ct} means the charge transfer resistance, and Z_w is the Warburg impedance [43]. The diffusion coefficient of Na^+ (D_{Na^+}) could be calculated by the following equation:

$$D_{Na^+}=R^2T^2/(2A^2n^4F^4C^2\sigma^2) \quad (1)$$

where R is the molar gas constant, T is the thermodynamic temperature, A is the surface area of the electrode, n stands for the number of transferred

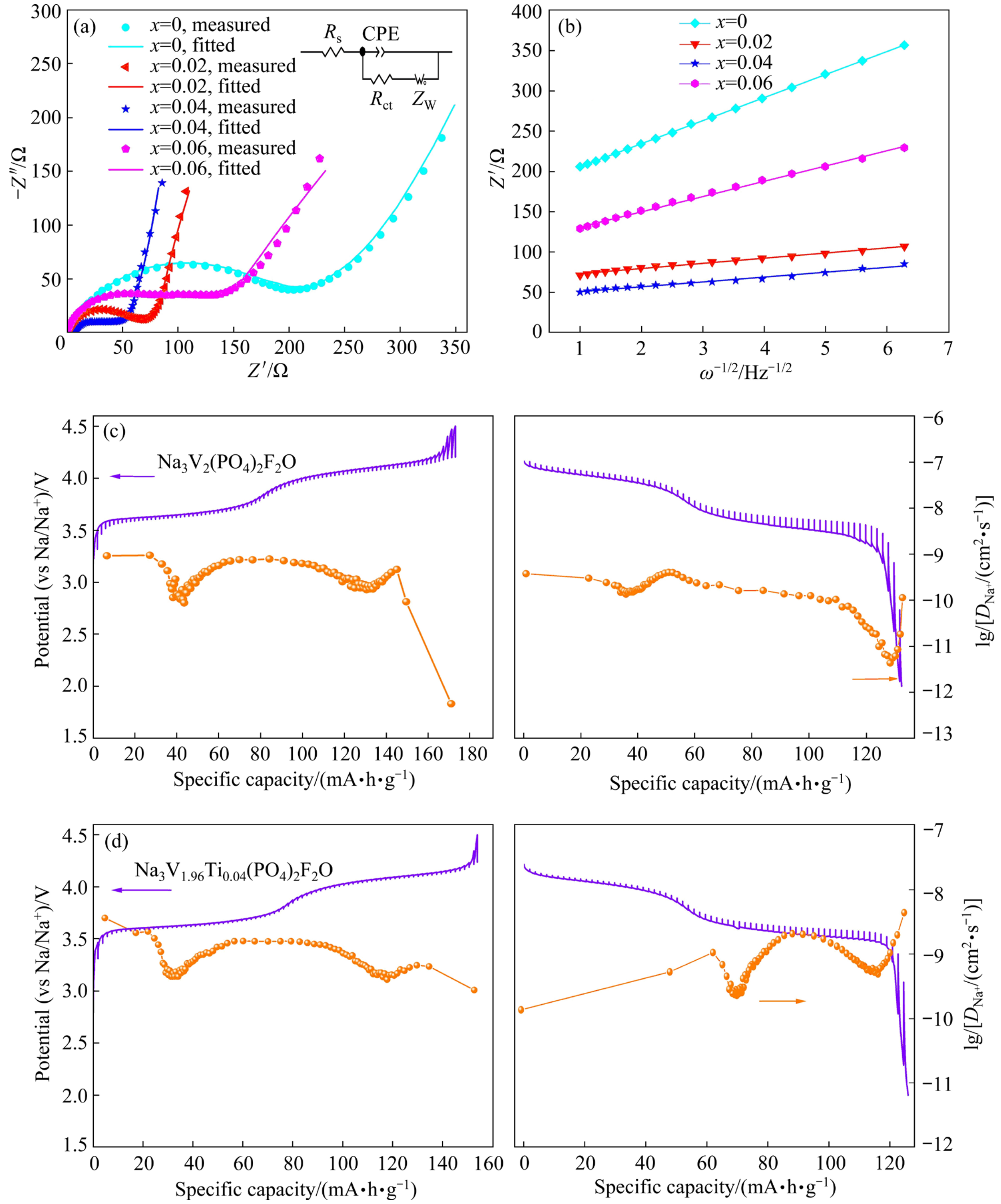

Fig. 8 Nyquist plots of $Na_3V_{2-x}Ti_x(PO_4)_2F_2O$ (x=0, 0.02, 0.04, 0.06) (a); Linear fitting of $Z'-\omega^{-1/2}$ from EIS (b); GITT curves with corresponding D_{Na^+} of pristine $Na_3V_2(PO_4)_2F_2O$ (c); GITT curves with corresponding D_{Na^+} of $Na_3V_{1.96}Ti_{0.04}(PO_4)_2F_2O$ (d)

electrons, F is the Faraday constant, C is the concentration of sodium ions, and σ is the Warburg coefficient that can be obtained from the slope of Z'–$\omega^{-1/2}$ as shown by the following equation:

$$Z'=R_s+R_{ct}+\sigma\omega^{-1/2} \quad (2)$$

where ω is the angular frequency in the lower frequency region. The linear relationship between Z' and $\omega^{-1/2}$ at low frequencies is depicted and simulated in Fig. 8(b). The finally calculated R_s, R_{ct} and D_{Na^+} are given in Table 3. It can be seen that $Na_3V_{1.96}Ti_{0.04}(PO_4)_2F_2O$ shows the smallest R_{ct} and the highest D_{Na^+}, indicating a noticeably enhanced electrochemical kinetics. Its D_{Na^+} (3.79×10^{-10} cm^2/s) is more than one order of magnitude higher than that of pristine NVPFO (2.83×10^{-11} cm^2/s), and is also remarkably higher than that of other doped samples.

Table 3 Calculation results from EIS spectra of different $Na_3V_{2-x}Ti_x(PO_4)_2F_2O$ samples

Sample	R_s/Ω	R_{ct}/Ω	D_{Na^+}/(cm^2·s^{-1})
x=0	7.80	191.08	2.83×10^{-11}
x=0.02	5.02	67.98	2.07×10^{-10}
x=0.04	4.37	43.13	3.79×10^{-10}
x=0.06	3.92	131.08	6.68×10^{-11}

Furthermore, GITT is used to analyze the variations of D_{Na^+} and electrochemical kinetics at different SOC (state of charge) and DOD (depth of discharge) during charging/discharging. The batteries are repeatedly charged (or discharged) for 10 min with a relaxation time of 60 min in between. According to the GITT technique, the D_{Na^+} can be calculated via the following equation:

$$D_{Na^+}=\frac{4}{\pi}\left(\frac{mV_M}{MS}\right)^2\left(\frac{\Delta E_s}{\Delta E_\tau}\right)^2 \quad (3)$$

where m is the mass of the electrode material, M is its molar mass, V_M is its molar volume, S is the contact area between the electrode and electrolyte, ΔE_s is the potential change of two adjacent steady states, and ΔE_τ is the steady potential change after a pulse electric current [46].

The GITT curves and the corresponding D_{Na^+} of pristine NVPFO and those of the optimized $Na_3V_{1.96}Ti_{0.04}(PO_4)_2F_2O$ are selected for comparison, and the results are shown in Figs. 8(c, d). The D_{Na^+} of pristine NVPFO roughly varies from 10^{-12} to 10^{-9} cm^2/s during charging/discharging, but that of $Na_3V_{1.96}Ti_{0.04}(PO_4)_2F_2O$ ranges from 10^{-10} to 10^{-8} cm^2/s. The values agree well with those obtained by EIS in Table 3. Therefore, $Na_3V_{1.96}Ti_{0.04}(PO_4)_2F_2O$ is verified again exhibiting fast Na^+ diffusion with rapid electrochemical kinetics during (de)sodiation. As a result, the battery performances especially the rate capability and cycling stability are remarkably improved.

4 Conclusions

(1) Ti is successfully doped into $Na_3V_2(PO_4)_2F_2O$ by partially substituting V during a facile solid-state preparation process. Similar to the oxidation states of vanadium, the doped Ti is also confirmed to exist in two states: Ti^{3+} and Ti^{4+}. The corresponding valances are advantageous for maintaining charge balance and structure stability. In doped $Na_3V_{2-x}Ti_x(PO_4)_2F_2O$ ($0\le x<1$), smaller crystallographic volumes are observed due to the smaller ionic radii of Ti^{3+} and Ti^{4+} when compared with V^{3+} and V^{4+}.

(2) The particle shape, size and surface carbon coating remain well-preserved after Ti doping. However, the electrochemical reduction peaks (discharge plateaus) are split from two to three due to the rearrangement of the local redox environment resulting from Ti doping.

(3) With an optimal doping amount of x=0.04, the electrochemical kinetics during charging/discharging is noticeably enhanced, and the Na^+ diffusion coefficient is more than an order of magnitude higher than that of its undoped counterpart.

(4) As a result, the rate capability especially the fast charge/discharge ability and the cycling stability of $Na_3V_2(PO_4)_2F_2O$ are remarkably improved. The optimized $Na_3V_{1.96}Ti_{0.04}(PO_4)_2F_2O$ is demonstrated to be a promising cathode material for sodium-ion batteries.

CRediT authorship contribution statement

Xiao-fei SUN: Conceptualization, Methodology, Formal analysis, Resources, Software, Writing − Original draft, Writing − Review & editing, Funding acquisition, Supervision, Project administration; **Anastase NDAHIMANA:** Investigation, Data curation, Validation, Software, Visualization, Writing − Original draft; **Ling-zhi WANG:** Data curation, Validation, Software, Visualization, Writing − Review & editing; **Zi-kang WANG:** Investigation, Validation; **Quan-sheng LI:** Software, Visualization; **Wei TANG:** Formal analysis, Resources, Supervision; **Min-xing YANG:** Software; **Xue-song MEI:** Resources, Supervision.

Declaration of competing interest

The authors declare that they have no known competing financial interests or personal relationships that could have appeared to influence the work reported in this paper.

Acknowledgments

This work is financially supported by the National Natural Science Foundation of China (Nos. 52275463, 51772240), the Key Research and Development Projects of Shaanxi Province, China (Nos. 2018ZDXM-GY-135), and the National Key Research and Development Program of China (Nos. 2021YFB3302000). The Instrumental Analysis Center of Xi'an Jiaotong University is acknowledged for technical help on structure characterization.

References

[1] DEHGHANI-SANIJ A R, THARUMALINGAM E, DUSSEAULT M B, FRASER R. Study of energy storage systems and environmental challenges of batteries [J]. Renewable & Sustainable Energy Reviews, 2019, 104: 192−208.

[2] OLABI A G, ONUMAEGBU C, WILBERFORCE T, RAMADAN M, ABDELKAREEM M A, AL-ALAMI A H. Critical review of energy storage systems [J]. Energy, 2021, 214: 118987.

[3] WU Fei-xiang, MAIER J, YU Yan. Guidelines and trends for next-generation rechargeable lithium and lithium-ion batteries [J]. Chemical Society Reviews, 2020, 49: 1569−1614.

[4] GOODENOUGH J B, PARK K S. The Li-ion rechargeable battery: A perspective [J]. Journal of the American Chemical Society, 2013, 135: 1167−1176.

[5] SUN Xiao-fei, HOU Xiang-guo, MEI Xue-song, HAN Yan-bin, LIU Bin, LI Quan-sheng, WANG Zi-kang, TANG Wei, WU Yu-ping, WANG Wen-jun, CUI Jian-lei. Ultrafast laser drilling of 3D porous current collectors for high-capacity electrodes of rechargeable batteries [J]. ACS Sustainable Chemistry & Engineering, 2023, 11: 7357−7366.

[6] ARMAND M, TARASCON J M. Building better batteries [J]. Nature, 2008, 451: 652−657.

[7] TIAN Yao-sen, ZENG Guo-bo, RUTT A, SHI Tan, KIM H, WANG Jing-yang, KOETTGEN J, SUN Ying-zhi, OUYANG Bin, CHEN Tina, LUN Zheng-yan, RONG Zi-qin, PERSSON K, CEDER G. Promises and challenges of next-generation "Beyond Li-ion" batteries for electric vehicles and grid decarbonization [J]. Chemical Reviews, 2021, 121: 1623−1669.

[8] SLATER M D, KIM D, LEE E, JOHNSON C S. Sodium-ion batteries [J]. Advanced Functional Materials, 2013, 23: 947−958.

[9] DELMAS C. Sodium and sodium-ion batteries: 50 years of research [J]. Advanced Energy Materials, 2018, 8: 1703137.

[10] QIN Mu-lan, LIU Wan-min, XIANG Yuan-jin, WANG Wei-gang, SHEN Bin. Synthesis and electrochemical performance of V_2O_5/NaV_6O_{15} nanocomposites as cathode materials for sodium-ion batteries [J]. Transactions of Nonferrous Metals Society of China, 2020, 30: 2200−2206.

[11] CHANG Yi-jiao, XIE Guang-hui, ZHOU Yong-mao, WANG Jie-xi, WANG Zhi-xing, GUO Hua-jun, YOU Bian-zheng, YAN Guo-chun. Enhancing storage performance of P2-type $Na_{2/3}Fe_{1/2}Mn_{1/2}O_2$ cathode materials by Al_2O_3 coating [J]. Transactions of Nonferrous Metals Society of China, 2022, 32: 262−272.

[12] YIN Xiu-ping, SARKAR S, SHI Shan-shan, HUANG Qiu-an, ZHAO Hong-bin, YAN Liu-ming, ZHAO Yu-feng, ZHANG Jiu-jun. Recent progress in advanced organic electrode materials for sodium-ion batteries: Synthesis, mechanisms, challenges and perspectives [J]. Advanced Functional Materials, 2020, 30: 1908445.

[13] HUANG Tian-bei, NIU Yu-bin, YANG Qiu-ju, YANG Wen-ting, XU Mao-wen. Self-template synthesis of prussian blue analogue hollow polyhedrons as superior sodium storage cathodes [J]. ACS Applied Materials & Interfaces, 2021, 13: 37187−37193.

[14] YUAN Yong, WEI Qing-yuan, YANG Shao-kang, ZHANG Xiao-yu, JIA Min, YUAN Jia-ren, YAN Xiao-hong. Towards high-performance phosphate-based polyanion-type materials for sodium-ion batteries [J]. Energy Storage Materials, 2022, 50: 760−782.

[15] DACEK S T, RICHARDS W D, KITCHAEV D A, CEDER G. Structure and dynamics of fluorophosphate Na-ion battery cathodes [J]. Chemistry of Materials, 2016, 28: 5450−5460.

[16] XU Shi-tan, YANG Yi, TANG Fang, YAO Yu, LV Xiang, LIU Lin, XU Chen, FENG Yue-zhan, RUI Xian-hong, YU Yan. Vanadium fluorophosphates: Advanced cathode materials for next-generation secondary batteries [J]. Materials Horizons, 2023, 10: 1901−1923.

[17] SUN Xiao-fei, NDAHIMANA A, WANG Zi-kang, MEI Xue-song, LIU Bin, GAO Guo-xin, XIONG Li-long, WANG Hai-tao, WANG Wen-jun. Enhanced Na^+ diffusion in $Na_3V_2(PO_4)_2F_2O$ cathodes via Zr^{4+} doping for high-rate and long-cycling sodium batteries [J]. Journal of Alloys & Compounds, 2023, 945: 169314.

[18] SERRAS P, PALOMARES V, GOÑI A, KUBIAK P, ROJO T. Electrochemical performance of mixed valence $Na_3V_2O_{2x}(PO_4)_2F_{3-2x}$/C as cathode for sodium-ion batteries [J]. Journal of Power Sources, 2013, 241: 56−60.

[19] RAJAGOPALAN R, ZHANG Zheng-na, TANG You-gen, JIA Chuan-kun, JI Xiao-bo, WANG Hai-yan. Understanding crystal structures, ion diffusion mechanisms and sodium storage behaviors of NASICON materials [J]. Energy Storage Materials, 2021, 34: 171−193.

[20] HE Jia-rong, TAO Tao, YANG Fan, SUN Zhi-peng. Manipulating the phase compositions of $Na_3(VO_{1-x}PO_4)_2F_{1+2x}$ $(0\leq x\leq 1)$ and their synergistic effects with reduced

graphene oxide toward high-rate sodium-ion batteries [J]. ACS Applied Materials & Interfaces, 2021, 13: 60099−60114.

[21] LIANG Kang, ZHAO Hong-shun, LI Jian-bin, HUANG Xiao-bing, JIA Shu-yong, CHEN Wen-kai, REN Yu-rong. Engineering crystal growth and surface modification of $Na_3V_2(PO_4)_2F_3$ cathode for high-energy-density sodium-ion batteries [J]. Small, 2023, 19: 2207562.

[22] GU Zhen-yi, GUO Jin-zhi, ZHAO Xin-xin, WANG Xiao-tong, XIE Dan, SUN Zhong-hui, ZHAO Chen-de, LIANG Hao-jie, LI Wen-hao, WU Xing-long. High-ionicity fluorophosphate lattice via aliovalent substitution as advanced cathode materials in sodium-ion batteries [J]. InfoMat, 2021, 3: 694−704.

[23] XIONG Fang-yu, LI Jian-tao, ZUO Chun-li, ZHANG Xiao-lin, TAN Shuang-shuang, JIANG Ya-long, AN Qin-you, CHU P K, MAI Li-qiang. Mg-doped $Na_4Fe_3(PO_4)_2$-(P_2O_7)/C composite with enhanced intercalation pseudo-capacitance for ultra-stable and high-rate sodium-ion storage [J]. Advanced Function Materials, 2023, 33: 2211257.

[24] WANG Mei-yi, ZHAO Xin-xin, GUO Jin-zhi, NIE Xue-jiao, GU Zhen-yi, YANG Xu, WU Xing-long. Enhanced electrode kinetics and properties via anionic regulation in polyanionic $Na_{3+x}V_2(PO_4)_{3-x}(P_2O_7)_x$ cathode material [J]. Green Energy & Environment, 2022, 7: 763−771.

[25] YIN Ya-meng, PEI Cun-yuan, LIAO Xiao-bin, XIONG Fang-yu, YANG Wei, XIAO Biao-biao, ZHAO Yan, REN Zi-jie, XU Long-hua, AN Qin-you. Revealing the multi-electron reaction mechanism of $Na_3V_2O_2(PO_4)_2F$ towards improved lithium storage [J]. ChemSusChem, 2021, 14: 2984−2991.

[26] LI Yu, CHEN Ming-hua, LIU Bo, ZHANG Yan, LIANG Xin-qi, XIA Xin-hui. Heteroatom doping: An effective way to boost sodium ion storage [J]. Advanced Energy Materials, 2020, 10: 2000927.

[27] ZHUANG Shu-han, YANG Chun-chuen, ZHENG Ming-tao, RENGAPILLAI S, MARIMUTHU S, CHIANG Yu-shen, CHANG B K, HUANG Chia-hung, LIU Wei-ren. A combined first principles and experimental study on Al-doped $Na_3V_2(PO_4)_2F_3$ cathode for rechargeable Na batteries [J]. Surface & Coatings Technology, 2022, 434: 128184.

[28] CRIADO A, LAVELA P, PÉREZ-VICENTE C, ORTIZ G F, TIRADO J L. Effect of chromium doping on $Na_3V_2(PO_4)_2$-F_3@C as promising positive electrode for sodium-ion batteries [J]. Journal of Electroanalytical Chemistry, 2020, 856: 113694.

[29] YUE Li-juan, PENG Chao, GUO Chun-li, ZHOU Xin-yuan, LI Gang, WANG Na-na, ZHANG Jian-sheng, LIU Jia-qing, BAI Zhong-chao, ZHAO Xiu-song. $Na_3V_{2-x}Fe_x(PO_4)_2O_2F$: An advanced cathode material with ultra-high stability for superior sodium storage [J]. Chemical Engineering Journal, 2022, 441: 136132.

[30] SUN Xiao-fei, WANG Zi-kang, HU Qiong-dan, MEI Xue-song, ZHAO Yue, NDAHIMANA A, GENG Tao, CUI Jian-lei. Oxygen-tuned $Na_3V_2(PO_4)_2F_{3-2y}O_{2y}$ ($0 \le y < 1$) as high-rate cathode materials for rechargeable sodium batteries [J]. ACS Applied Energy Materials, 2022, 5: 15799−15808.

[31] LI Xin, KONG Qing-quan, AN Xu-guang, ZHANG Jing, WANG Qing-yuan, YAO Wei-tang. Enhanced cycling stability and storage performance of $Na_{0.67}Ni_{0.33}Mn_{0.67-x}$-$Ti_xO_{1.9}F_{0.1}$ cathode materials by Mn-rich shells and Ti doping [J]. Journal of Colloid and Interface Science, 2023, 633: 82−91.

[32] SUN Xiao-fei, XU You-long, CHEN Guo-gang, DING Peng, ZHENG Xiao-yu. Titanium doped $LiVPO_4F$ cathode for lithium ion batteries [J]. Solid State Ionics, 2014, 268: 236−241.

[33] TONG Shuai, PAN Hui, LIU Hang, ZHANG Xiao-yu, LIU Xiang-yu, JIA Min, KANG Ya-hao, YUAN Yong, DU Xin-yi, YAN Xiao-hong. Titanium doping induced the suppression of irreversible phase transformation at high voltage for V-based phosphate cathodes of Na-ion batteries [J]. ChemSusChem, 2023, 16: e202300244.

[34] HUANG Yang-yang, LIA Xiang, WANG Jin-song, MIAO Lin, LI Chang, HAN Jian-tao, HUANG Yun-hui. Superior Na-ion storage achieved by Ti substitution in $Na_3V_2(PO_4)_3$ [J]. Energy Storage Materials, 2018, 15: 108−115.

[35] BUI K M, DINH V A, OKADA S, OHNO T. Hybrid functional study of the NASICON-type $Na_3V_2(PO_4)_3$: Crystal and electronic structures, and polaron-Na vacancy complex diffusion [J]. Physical Chemistry Chemical Physics, 2015, 17: 30433−30439.

[36] SONG Wen-chen, LI Hong, ZHU Fu-xing, LI Kun, ZHENG Quan. Extraction of vanadium from molten vanadium bearing slag by oxidation with pure oxygen in the presence of CaO [J]. Transactions of Nonferrous Metals Society of China, 2014, 24: 2687−2694.

[37] PALOMARES V, ITURRONDOBEITIA A, SANCHEZ-FONTECOBA P, GOONETILLEKE D, SHARMA N, LEZAMA L, ROJO T. Iron-doped sodium–vanadium fluorophosphates: $Na_3V_{2-y}O_{2-y}Fe_y(PO_4)_2F_{1+y}$ ($y<0.3$) [J]. Inorganic Chemistry, 2020, 59: 854−862.

[38] SUN Xiao-fei, HU Qiong-dan, TAO Tie-tuo, NDAHIMANA A, QI Lin, LI Quan-sheng, LIU Bin, MEI Xue-song. Improved battery performance of Fe-doped $LiVPO_4F$ with high capacity and stable cycling [J]. Materials Letters, 2021, 286: 129225.

[39] LIANG Kang, ZHAO Hong-shun, LI Jian-bin, HUANG Xiao-bing, Ren Yu-rong. High-performance $Na_3V_2(PO_4)_2F_3$ cathode obtained by a three-in-one strategy for self-sodium compensation, interface modification, and crosslinked carbon coatings [J]. Applied Surface Science, 2023, 615: 156412.

[40] BROUX T, BAMINE T, FAUTH F, SIMONELLI L, OLSZEWSKI W, MARINI C, MÉNÉTRIER M, CARLIER D, MASQUELIER C, CROGUENNEC L. Strong impact of the oxygen content in $Na_3V_2(PO_4)_2F_{3-y}O_y$ ($0 \le y \le 0.5$) on its structural and electrochemical properties [J]. Chemistry of Materials, 2016, 28: 7683−7692.

[41] LIU Zhi-ming, WANG Xian-you, WANG Ying, TANG An-ping, YANG Shun-yi, HE Liang-fu. Preparation of $NaV_{1-x}Al_xPO_4F$ cathode materials for application of sodium-ion battery [J]. Transactions of Nonferrous Metals Society of China, 2008, 18: 346−350.

[42] KOSOVA N V, REZEPOVA D O, MONTROUSSIER N. Effect of La^{3+} modification on the electrochemical performance of $Na_3V_2(PO_4)_2F_3$ [J]. Batteries-Basel, 2018, 4:

32.

[43] CHENG Jun, CHEN Yan-jun, SUN Shi-qi, TIAN Ze-yi, LINGHU Yao-yao, TIAN Zhen, WANG Chao, HE Zhen-feng, GUO Li. $Na_3V_2(PO_4)_3/C\cdot Na_3V_2(PO_4)_2F_3/C@RGO$ blended cathode material with elevated energy density for sodium ion batteries [J]. Ceramics International, 2021, 47: 18065−18074.

[44] KUMAR P R, JUNG Y H, WANG J E, KIM D K. $Na_3V_2O_2(PO_4)_2F$-MWCNT nanocomposites as a stable and high rate cathode for aqueous and non-aqueous sodium-ion batteries [J]. Journal of Power Sources, 2016, 324: 421−427.

[45] MA Cai-yun, XU Ting-ting, YAN Cong-cong, XU Jun-min, KONG De-zhi, ZHANG Zhuang-fei, SHEN Wei-xia, SHI Yu-meng, KE Chang, LI Xin-jian, WANG Ye. Mechanism investigation of high performance $Na_3V_2(PO_4)_2O_2F$/reduced graphene oxide cathode for sodium-ion batteries [J]. Journal of Power Sources, 2021, 482: 228906.

[46] HOU Yan, CHANG Kun, WANG Zhen-yu, GU Shuai, LIU Qiong, ZHANG Jun-jun, CHENG Hua, ZHANG Sheng-lin, CHANG Zhao-rong, LU Zhou-guang. Rapid microwave-assisted refluxing synthesis of hierarchical mulberry-shaped $Na_3V_2(PO_4)_2O_2F@C$ as high performance cathode for sodium & lithium-ion batteries [J]. Science China−Materials, 2019, 62: 474−486.

双价态 $Ti^{3+/4+}$掺杂提升 $Na_3V_2(PO_4)_2F_2O$ 钠正极的倍率与循环性能

孙孝飞 [1,2,3]，Anastase NDAHIMANA [1,2,3]，王凌志 [1,2]，王子康 [1,2]，
李泉省 [1,3]，唐 伟 [4]，杨敏行 [2,3]，梅雪松 [1,2,3]

1. 西安交通大学 机械制造系统工程国家重点实验室，西安 710049；
2. 西安交通大学 机械工程学院，西安 710049；
3. 西安交通大学 陕西省智能机器人重点实验室，西安 710049；
4. 西安交通大学 化学工程与技术学院，西安 710049

摘 要：利用双价态 $Ti^{3+/4+}$掺杂部分替代钒以改善 $Na_3V_2(PO_4)_2F_2O$ 的电化学性能。由于 $Ti^{3+/4+}$的离子半径较小，掺杂后 $Na_3V_2(PO_4)_2F_2O$ 的晶胞体积减小，并且 Ti 的氧化价态与 V 的价态一致。同时，Ti 掺杂引起充放电过程中 $Na_3V_2(PO_4)_2F_2O$ 局部氧化还原环境的重新排列，导致原本的 2 个放电平台(还原峰)分裂为 3 个。最优的 $Na_3V_{0.96}$-$Ti_{0.04}(PO_4)_2F_2O$ 在 0.1*C* 和 20*C* 倍率下的放电比容量分别为 123 和 63 mA·h/g, 在 0.5*C* 下循环 350 次后的容量保持率为 71.05%。电化学性能提升的主要原因在于掺杂后材料的充放电动力学大大增强，表明双价 $Ti^{3+/4+}$取代 $V^{3+/4+}$是钒基聚阴离子材料的一种有效改性策略。

关键词：氧代氟磷酸钒钠；Ti 掺杂；正极；钠电池；能量存储

(Edited by Bing YANG)